Limits on runoff episode duration for early Mars: integrating lake hydrology and climate models

Gaia Stucky de Quay[1], Timothy Andrew Goudge[1], Edwin Stephen Kite[2], Caleb I. Fassett[3], and Scott D. Guzewich[4]

[1]University of Texas at Austin
[2]University of Chicago
[3]Marshall Space Flight Center (NASA)
[4]NASA Goddard Spaceflight Center

November 22, 2022

Abstract

Fluvio-lacustrine features on the martian surface attest to a climate that was radically different in the past. Since climate models have difficulty sustaining a liquid hydrosphere at the surface, multiple cycles of runoff episodes may have characterized the ancient Mars climate. A fundamental question thus remains: what was the duration of these runoff-producing episodes? Here we use morphometric measurements from newly identified coupled lake systems (containing both an open- and a closed-basin lake). We combined hydrological balances with precipitation outputs from climate models, and found that breaching runoff episodes likely lasted 10ˆ2–10ˆ5 yr; other episodes may have been shorter but could not be longer. Runoff episode durations are model-dependent and spatially variable, and no climate model scenario can satisfy a unique duration for all coupled systems. In the near future, these quantitative constraints on early Mars lake persistence may be tested through in situ observations from Perseverance rover.

Limits on runoff episode duration for early Mars: integrating lake hydrology and climate models

Gaia Stucky de Quay[1,2], Timothy A. Goudge[1,2], Edwin S. Kite[3], Caleb I. Fassett[4], and Scott D. Guzewich[5]

[1]Jackson School of Geosciences, University of Texas at Austin, Austin, Texas 78712, USA
[2]Center for Planetary Systems Habitability, University of Texas at Austin, Austin, Texas 78712, USA
[3]Department of the Geophysical Sciences, University of Chicago, Chicago, Illinois 60637, USA
[4]NASA Marshall Space Flight Center, Huntsville, Alabama 35805, USA
[5]NASA Goddard Space Flight Center, Greenbelt, Maryland 20771, USA

Key Points:

- Coupled lake system morphologies were combined with climate model outputs to quantify upper and lower limits on runoff episode durations.
- Breaching runoff episodes lasted 10^2-10^5 yr depending on models and are spatially variable; other episodes could be shorter but not longer.
- Our constraints on lake persistence may be tested through *in situ* observations made by the Mars 2020 Perseverance rover in Jezero crater.

Corresponding author: Gaia Stucky de Quay, `g.stucky@utexas.edu`

Abstract

Fluvio-lacustrine features on the martian surface attest to a climate that was radically different in the past. Since climate models have difficulty sustaining a liquid hydrosphere at the surface, multiple cycles of runoff episodes may have characterized the ancient Mars climate. A fundamental question thus remains: what was the duration of these runoff-producing episodes? Here we use morphometric measurements from newly identified coupled lake systems (containing both an open- and a closed-basin lake). We combined hydrological balances with precipitation outputs from climate models, and found that breaching runoff episodes likely lasted $10^2 - 10^5$ yr; other episodes may have been shorter but could not be longer. Runoff episode durations are model-dependent and spatially variable, and no climate model scenario can satisfy a unique duration for all coupled systems. In the near future, these quantitative constraints on early Mars lake persistence may be tested through *in situ* observations from Perseverance rover.

1 Introduction

Constraining the duration of periods for which liquid water was present on the surface of Mars has remained a fundamental challenge since evidence for ancient fluvial activity was first discovered (Carr, 1987; Wordsworth, 2016; Kite, 2019). In addition to informing our understanding of planetary and climatic evolution, these hydrologic timescales have profound implications for potential habitability beyond Earth. Yet, the persisting difficulty in quantifying past timescales is two-fold. First, the duration of Mars' early hydroclimate can be assessed via different approaches, namely geomorphic analyses (e.g., Hoke et al., 2011), numerical climate models (e.g., Ramirez et al., 2020), or chemical alteration studies (e.g., Bishop et al., 2018). Although this should ideally work as an advantage, general agreement between these approaches is often lacking. Second, it is unlikely that a single, uniform ancient climate existed. Instead, early Mars was probably characterized by a dynamic climate with runoff episodes varying at shorter length- and timescales, as suggested by layered deposits, valley morphologies, semi-arid basin hydrology, and weak aqueous alteration, among others (e.g., Malin & Edgett, 2000; Barnhart et al., 2009; Matsubara et al., 2011; Ehlmann et al., 2011, respectively). Hence, convergence towards a constrained timescale solution requires not only an improved understanding of the spatio-temporal complexity of the hydroclimate, but also a shift towards viewing different timescale-deducing methods as complementary rather than contrasting.

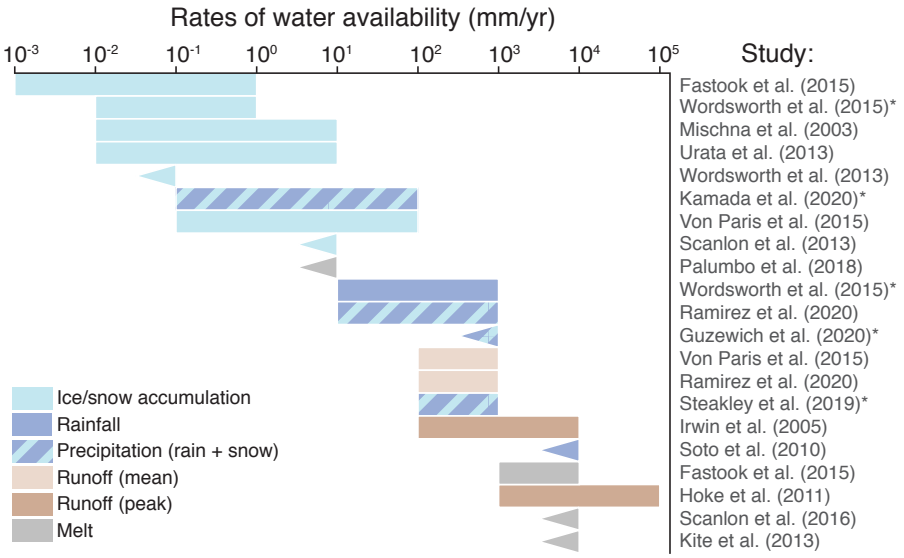

Figure 1. Range of water availability rates for early Mars from previous studies. Runoff rates are derived from geological observations and all other rates are from (climate/glacial) numerical models. Model outputs indicated with an asterisk are used in this work. Values are rounded to the nearest order of magnitude (see Supplementary Tables S1 and S2).

In general, most geomorphic evidence suggests a wet climate lasting at least 10 kyr, and perhaps 100 Myr, up to the Noachian-Hesperian boundary ($\gtrsim$ 3.7 Ga), whether inferred from erosional (e.g., Craddock & Howard, 2002; Barnhart et al., 2009) or depositional (e.g., Armitage et al., 2011; Schon et al., 2012; Grotzinger et al., 2015) systems. In order to align these geomorphic constraints with hydroclimatic limits set by geochemical records and climate models, it is often proposed that surface liquid water was episodic, although the mechanism behind this episodicity remains uncertain (Wordsworth, 2016; Kite, 2019). An important point that goes into this hypothesis is that geomorphic timescales are cumulative, i.e., they record the total amount of time taken to create a landform, whether a bedrock valley or fan deposit. As such, these studies typically rely on assumptions for runoff intermittency to calculate total durations (e.g., Buhler et al., 2014). If no hiatuses are considered, local depositional timescales could be substantially shorter (1-100 yr; e.g., Jerolmack et al., 2004; Fassett & Head, 2005; Kleinhans et al., 2010). Further, calculated water availability rates, such as precipitation, runoff, and melting rates, vary over several orders of magnitude (Figure 1); these estimates are not only sensitive to the methodology used, but also the spatial and temporal resolution employed. Clearly, there remains a need

to shed further light on the uninterrupted availability of liquid water on the martian surface. Here we aim to provide new insights into this problem by addressing the following question: how can we constrain the duration of a single runoff episode?

Our approach focuses on valley network-fed paleolakes, which provides a unique opportunity to assess individual surface runoff episodes: a discrete episode of time with net average positive runoff (i.e., runoff rate exceeds any losses; Supplementary Figure S1). Lake systems fall into one of two broad hydrological categories: open- or closed-basins (Cabrol & Grin, 1999, 2001; Fassett & Head, 2008; Goudge et al., 2015, 2016). Open-basin lakes accumulated enough water to overflow and erode an outlet canyon (e.g., Goudge et al., 2019), whereas closed-basin lakes did not. As such, the presence or absence of an outlet canyon directly records whether a threshold event—lake overspill—was achieved in any single runoff episode (Figure S1; Supplementary Text S1). Water input cannot be considered cumulative if separated by periods of water loss. In this work we capitalize on this threshold relationship by investigating newly identified coupled lake systems, which contain both an open- and a closed-basin lake that are hydrologically connected (Figure 2a; Stucky de Quay et al., 2020). By combining these new geological constraints with a suite of runoff rates from existing climate models, we are able to place new limits on runoff episode duration across the surface of ancient Mars.

2 Methodology

2.1 Paleolake geometry mapping

We investigated a subset of valley network-fed coupled paleolakes from Stucky de Quay et al. (2020), which, for both open- and closed-basin lakes contained within a coupled system, provide lake basin area (A_L), lake basin volume (V_L), and watershed area (A_W; Figure 2b). We used 7 coupled lake systems from this morphologic database (Supplementary Figure S2; Table S3) and measured an additional fourth parameter for all systems: lake volume remaining after the open-basin lake breached and drained, V_R. This was done by identifying the highest closed contour in the basin before it spilled into the outlet canyon (e.g., Fassett & Head, 2008). For this we used the ∼100 m/pixel global daytime infrared mosaic (Edwards et al., 2011) from the Thermal Emission Imaging System (THEMIS; Christensen et al., 2004), and ∼463 m/pixel Mars Orbiter Laser Altimeter global gridded elevation data (MOLA; Smith et al., 2001). Subsequently, coupled systems were classified as either embedded (where

the open-basin lake is contained within the watershed of the closed-basin lake watershed; n=6) or adjacent (where the open- and closed-basin lake watersheds share drainage divides; n=1). Importantly, sediment deposition—before, during, or after lake filling—is unlikely to significantly affect measured basin morphologies (see Supplementary Text S2; Mangold et al., 2009).

2.2 Derivation of lake hydrological balance

Paleolake hydrology can be expressed using standard water balance equations (Horton, 1943; Benson & Thompson, 1987; Howard, 2007; Fassett & Head, 2008; Matsubara et al., 2011). In a simplified system, the total lake volume, V_L, accumulated over a runoff episode of duration, T, is given by

$$V_L = ((A_L + A_W)P - (A_L)E)T, \tag{1}$$

where P is average rainfall and/or snowmelt rates and E is average evaporation rate. Since lakes are fed by valley networks (Figure 1; Figure S2), this implies they were predominantly fed by surface runoff, and groundwater infiltration is likely to have limited effect on hydrology (see Stucky de Quay et al., 2020). In an embedded coupled system where an upstream open-basin lake (O) breaches at a time, T_B, and overflows into a downstream closed-basin lake (C), and assuming a steady and uniform precipitation rate, we can express both lake volumes as a function of time, t:

$$v_O = \begin{cases} V_{L,O}\left(\dfrac{t}{T_B}\right) & \text{if } t \leq T_B; \\ V_R & \text{if } t > T_B; \end{cases} \tag{2}$$

$$v_C = \begin{cases} (A_{W,C} - XA_{L,C})\dfrac{V_{L,O}}{A_{W,O} - XA_{L,O}}\left(\dfrac{t}{T_B}\right) & \text{if } t \leq T_B; \\ (A_{W,O} + A_{W,C} - XA_{L,O} - XA_{L,C})\dfrac{V_{L,O}}{A_{W,O} - XA_{L,O}}\left(\dfrac{t}{T_B}\right) - V_R & \text{if } t > T_B, \end{cases} \tag{3}$$

where the full derivation is provided in Supplementary Text S3. Here, X denotes the aridity of the system, and can be expressed as $(\frac{1}{\text{AI}} - 1)$, where the aridity index, AI, is the ratio of runoff to evaporation (P/E; Matsubara et al., 2011; Stucky de Quay et al., 2020). Because closed-basin lakes did not overflow, the observed basin volume provides an upper limit for v_C, i.e., v_C in equation (3) cannot exceed $V_{L,C}$. These expressions allow us to assess the permitted timescales for runoff generation, which must be greater than the breaching timescale, T_B, but less than the maximum timescale, T_{max} (where $v_C[T_{max}] = V_{L,C}$; see Figure S1).

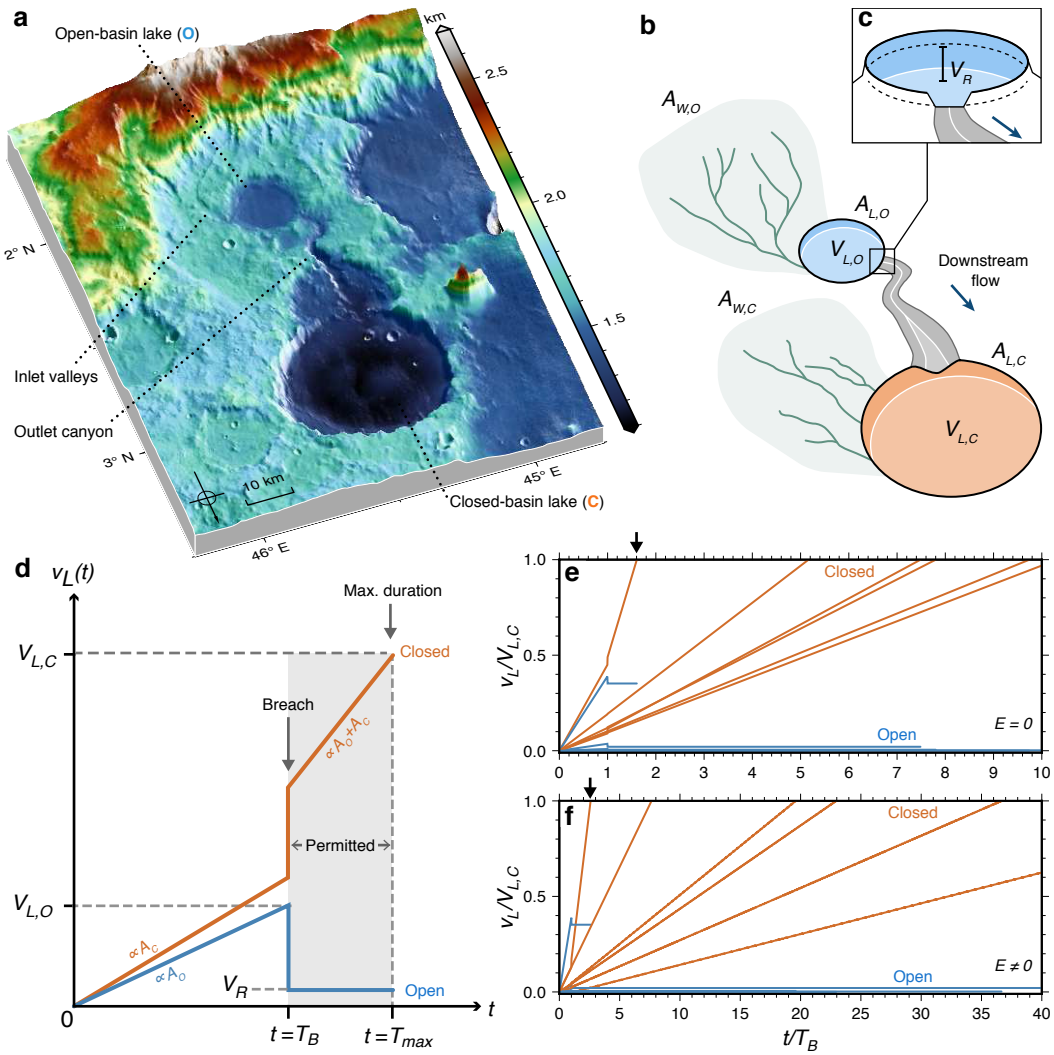

Figure 2. (a) Example of a coupled lake system on Mars (Basin ID 185/89; Table S3). Images and elevation data are from THEMIS and MOLA, respectively. (b) Schematic diagram of key lake morphometric measurements. Blue polygon = open-basin lake (O) with area $A_{L,O}$ and volume $V_{L,O}$; orange polygon = closed-basin lake (C) area $A_{L,C}$ and volume $V_{L,C}$. Green shaded area = watershed areas, $A_{W,O}$ and $A_{W,C}$) where dark green=inlet valleys. Grey polygon = outlet canyon. (c) Schematic of remaining lake volume V_R after breach and outlet erosion (Figure 2c). (d) Simple model for lake volume changes over time following equations (2) and (3). Gray shaded region denotes the permitted runoff episode duration between breaching (T_B) and the maximum duration set by the volume of the closed-basin lake (T_{max}). Here, $A_O = A_{W,O} + A_{L,O}$ and $A_C = A_{W,C} + A_{L,C}$ for simplicity. (e) and (f) show results using our 6 embedded coupled systems, where (e) considers no evaporation, and (f) applies an aridity index, AI, of ~ 0.26. Here, time (x-axis) is normalized to the breach event, T_B, and volume (y-axis) is normalized to the volume of each individual closed-basin lake ($V_{L,C}$). Black arrow = the shortest T_{max}/T_B value, indicating the most restrictive case.

Figure 2d shows the predicted changes in lake volume for open- and closed-basin lakes schematically following equations (2) and (3). Both lakes fill at a rate proportional to their initial catchment size. At $t = T_B$, a breach occurs in the upstream open-basin lake and the drained volume is transferred downstream into the closed-basin lake. After the breach, the open-basin lake volume remains constant and the closed-basin lake has a higher filling rate equivalent to the combined catchments of both lakes (since inflow and outflow in the upstream open-basin lake are now balanced). Without independent constraints, these runoff episode limits can only be constrained relative to the breaching timescale.

2.3 Temporal constraints using climate models

To provide absolute constraints on the runoff episode duration, we derived the lower, T_B, and upper, T_{max}, limits by building on the expressions provided above (equations 1-3; Text S3; Figure S1). For a given embedded coupled system containing an open- and closed-basin lake, the runoff episode limits are given as

$$T_B = \frac{V_{L,O}}{(A_{W,O} - XA_{L,O})P}; \tag{4}$$

$$T_{max} = \frac{V_{L,C} + V_R}{(A_{W,O} + A_{W,C} - XA_{L,O} - XA_{L,C})P}. \tag{5}$$

To explicitly solve for these durations, we use precipitation rates from existing climate model outputs as a proxy for P. Out of the existing constraints outlined in Figure 1, we selected precipitation rate outputs from four global climate models based on data availability and their full coverage of the planet (Figures 3a-d; Wordsworth et al., 2015; Steakley et al., 2019; Kamada et al., 2020; Guzewich et al., 2021). For each coupled lake system, we extracted the average value for P within the total lake watershed using outputs from each of the models (Figure 3e). Note that each model considered various different scenarios, resulting in a total of 16 model outputs (Supplementary Table S4). This provides, for each coupled lake system, a range of durations that are permitted both by its morphology and the regional, model-dependent runoff rate.

3 Results

3.1 Relative runoff episode limits

The geometries of paleolakes allow us to assess a range of timescales for which a given coupled system could have remained active after breaching of the open-basin lake. Figures

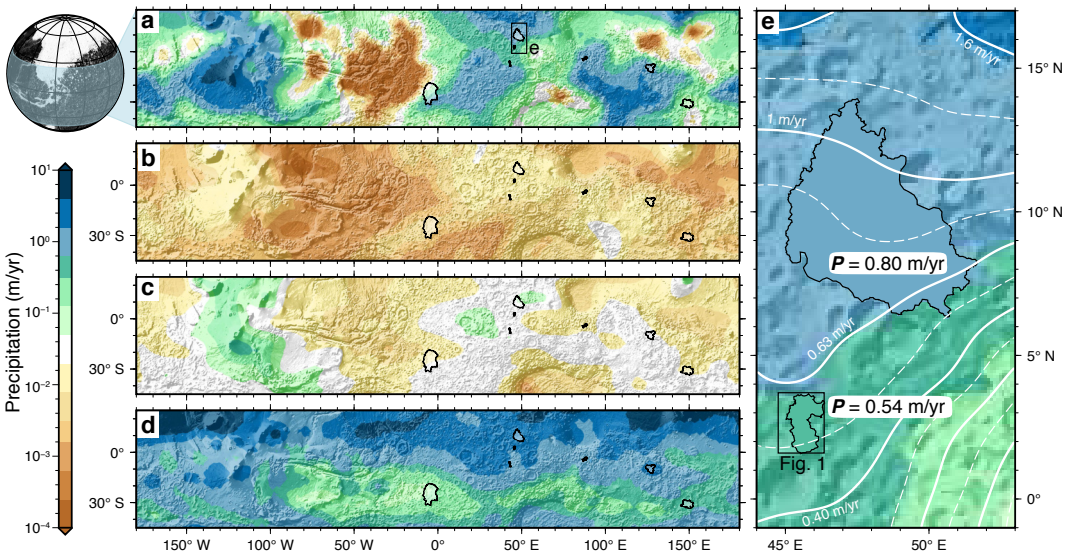

Figure 3. Precipitation rates from global climate models and watershed data extraction. Four climate model outputs are shown: (a) Warm and wet climate from Wordsworth et al. (2015). Note location of panel (e). (b) 0.5 bar atmosphere scenario from Kamada et al. (2020). (c) 10 m global equivalent layer (GEL) of water at 25° obliquity from Guzewich et al. (2021). (d) An impact-heated atmosphere generated by a 50 km-diameter impactor from Steakley et al. (2019). Table S4 lists all 16 climate scenarios. Black polygons = total watershed of lake systems. Latitudes and longitudes are the same for (a)-(d). (e) Example calculation of regional runoff rate, P, for each system, which is averaged across the combined watershed and lake area. Hillshade from MOLA topography.

2e,f show the relative runoff episode durations that are permitted for all 6 embedded coupled systems. Note that only values between $t = T_B$ and T_{max} (i.e., gray shaded region in Figure 2d) are permitted; hence, systems with a large value of T_{max}/T_B have a wide range of permitted runoff episode durations, whereas systems that have $T_{max}/T_B \rightarrow 1.0$ imply a narrow range of permitted timescales relative to breaching. Values for T_{max}/T_B range from 1.6 to 10 if we assume no evaporation occurs (Figure 2e). If we assume a more realistic semiarid regime, with AI ~ 0.26 (from Stucky de Quay et al., 2020), then T_{max}/T_B ranges between 2.6 to 63 (Figure 2f).

These results suggest that, for the most tightly constrained system (i.e., the lowest T_{max}/T_B value; black arrow in Figure 2e,f), runoff generation can only continue for $\sim 1.6-2.6$ longer than the time it took to initially breach the open-basin lake. For this system (Basin ID 187/9; Table S3), the open-basin lake spends a minimum of $\sim 40\%$ of the runoff

episode duration filling up before it breaches. Systems with larger T_{max}/T_B values may not require runoff cessation shortly after breaching, but do not explicitly preclude it. As a result, open lake systems on Mars may spend a large portion of their evolution filling up as closed lakes, as opposed to as stable open lakes.

3.2 Distribution of absolute runoff episode durations

Using equations (4) and (5), we solved for T_B and T_{max} for each of the seven coupled systems using existing P values extracted from global climate models (Figure 3; Table S4). The resultant distributions for the runoff episode durations are shown in Figure 4. Each panel in Figure 4 illustrates the number of coupled systems with T_B and T_{max} values that bound the episode duration, T, specified on the x-axis (i.e., systems where $T_B \leq T < T_{max}$ is satisfied) for that climate scenario. As a reference, Figure 4a shows the permitted temporal distributions if we assume globally constant runoff rates from geological observations by Irwin et al. (2005). Here, a 10,000 yr runoff episode duration only satisfies one coupled system if the runoff rate was 60 mm/d, but would satisfy three systems if it was 1 mm/d. Each remaining panel (b-f) shows the timescale distributions for four different global climate studies, including different scenarios within each to explore how various parameters affect timescale distributions (Table S4). Notably, none of the models satisfy all 7 coupled systems for a single duration bin (see Section 4.1).

Figure 4b compares timescales using two end-member precipitation scenarios for rainfall and snowfall (wet, warm at 1.0 bar vs. cold, icy at 0.6 bar, respectively, from Wordsworth et al., 2015). Figure 4c shows the effect of increasing surface pressure (from 0.5 to 2.0 bar; Kamada et al., 2020). Climate scenarios with higher pressures, and consequently greater rainfall, generally result in shorter timescales, except for the highest surface pressure of 2.0 bar, where timescales increase. Using model outputs from Guzewich et al. (2021), we find that higher obliquities result in reduced runoff episode durations; however, global equivalent water inventory size has negligible effects (Figures 4d,e). Finally, durations required for an impact-induced atmosphere in Figure 4f show that impactor size does not significantly affect the distributions (50 and 100 km-diameter; Steakley et al., 2019). The distributions in Figure 4 assume a semiarid regime with AI ~ 0.26, however results with no evaporation are also shown in Supplementary Figure S3, suggesting less than an order of magnitude difference.

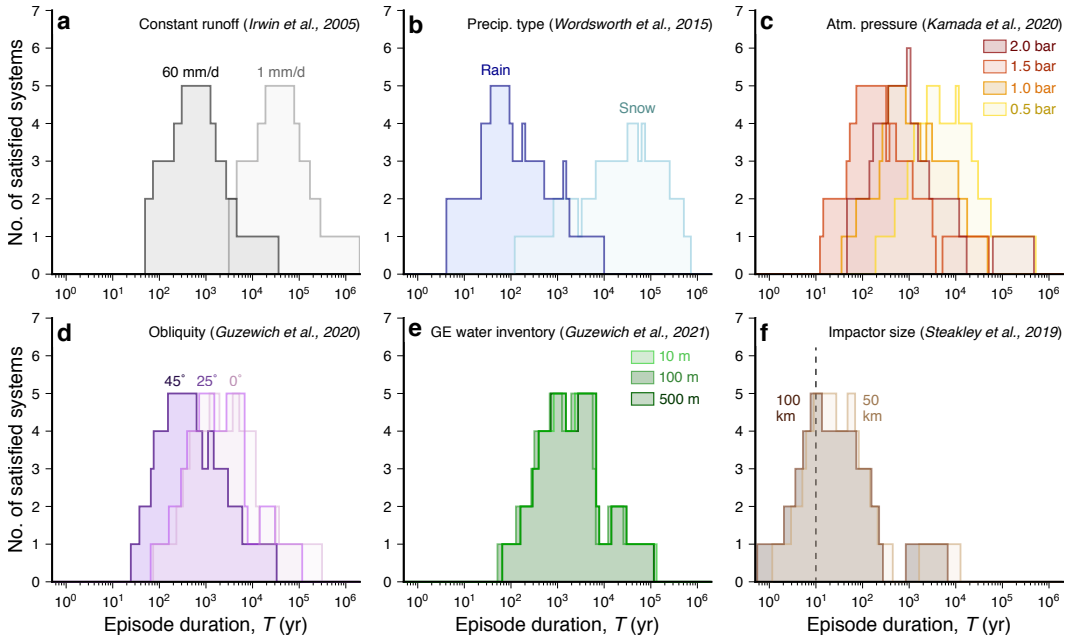

Figure 4. Distribution of runoff episode durations that satisfy the 7 studied coupled systems using different runoff constraints: (a) Spatially constant runoff rate (Irwin et al., 2005); (b)–(f) Precipitation rate outputs from different climate models/scenarios as indicated above each panel (Table S4); GE = global equivalent; precip. = precipitation; atm. = atmospheric; dashed line in (f) = limit of 10 years, the duration for which cumulative precipitation was estimated in the impact heating scenario.

4 Discussion & Conclusion

4.1 Implications for ancient hydroclimate scenarios

The mere existence of coupled lake systems implies that runoff generation was sufficiently intense and/or prolonged such that the contained open-basin lake breaches, but not enough to breach the downstream closed-basin lake (Figure 2). Unlike most terrestrial systems, these lakes would be less capable of achieving steady-state because the flat-floored, steep-walled crater basins would not allow lake area to continually increase until enhanced evaporation could offset runoff input. These systems thus point to a climate regime that comprises lake filling and overflow, followed—sometimes shortly—by runoff cessation, all within the timeframes indicated by Figure 4.

Overall, the shortest runoff episode durations (<1 yr) are observed for the 100 km-diameter impact heating scenario from Steakley et al. (2019), whereas the longest durations

correspond to Wordsworth et al. (2015)'s snowfall scenario (up to 10^6 yr; see following section for discussion on snowfall vs. snowmelt). In addition to the relative position of each distribution in Figure 4, both the width and height of each individual distribution provide further information. The wider the distribution, the larger the total range of timescales that are permitted by coupled lake hydrology. The taller the distribution (where maximum = 7), the greater the number of lakes that are satisfied by any given runoff episode duration bin. As such, the peak of each distribution denotes the T bin that satisfies the most coupled lake systems. If all systems were formed in runoff episodes of similar durations, then this peak T bin corresponds to the most probable duration for that climate scenario's distribution.

Distributions of T tend to span 3–4 orders of magnitude, suggesting a wide range of permissible timescales for all scenarios. When assessing the distribution peaks, we find that no single T bin can satisfy all 7 coupled systems for any scenario. Most scenarios can satisfy up to 5 systems, with the two exceptions being the 2.0 bar scenario from Kamada et al. (2020), which satisfies 6 systems for $T \sim 1000$ yr, and the Wordsworth et al. (2015) snowfall scenario which only satisfies 4 at most (Figure 4). In general, most distribution peaks lie between 100 – 10,000 yr, suggesting this range of breaching episode duration satisfies the greatest number of coupled system hydrologic constraints across the planet. Importantly, other runoff episodes (either before or after the breaching episode; Figure S1) could have been shorter, but no episode could exceed the maximum durations at any point in during early Mars' history, since closed-basin lakes did not overflow.

4.2 Runoff rates and the geological record

Global climate models provide valuable quantitative inputs for assessing runoff rates required to fill our lake systems as a function of space. Although geological estimates are important for understanding reach-scale, channel-forming hydrology, they are more challenging to extend over regional- to global-scales precisely due to being both localized and related to peak hydrologic conditions (Figure 1; Table S2). For example, at first glance runoff rates modeled by Steakley et al. (2019) most closely match those estimated from geomorphic observations (Figure 1). However, such an impact-heated atmosphere can only persist for a maximum ∼10 yr (Steakley et al., 2019; Turbet et al., 2020), and systems requiring longer time periods are not permissible. Despite this cut-off, the runoff rates provided are sufficient to fill the lakes, and are able to satisfy 5 systems for a runoff episode duration ∼10 yr (Figure 4f). Importantly, though, for discrete events such as an impact,

it seems most likely that T was spatially homogeneous, as it would reflect a global heating event.

Aside from the precipitation models used in this study (Figure 4), others have also explored snowfall or ice accumulation rates as a function of space (Figure 1). These snow/ice accumulation distributions are commonly compared to locations of fluvio-lacustrine features such as valley networks (e.g., Wordsworth et al., 2015). However, the relationship between snow accumulation and subsequent runoff rates is not well understood, and variability in processes such as snow ablation could result in spatial discrepancies between snowfall and resulting runoff. Other studies have derived snowmelt production rates (Figure 1), however, when calculated in global models they have yet to generate sufficient runoff in the required mid-latitude regions (e.g., Palumbo & Head, 2018). This could explain why the snowfall distribution in Figure 4b satisfies less systems than all other models for a single time bin, since the duration of liquid water availability (e.g., snowmelt) may not be directly related to snow/ice accumulation at any given location.

4.3 Lake persistence and episodic climate forcing

Despite the wide range of climate scenarios invoked, our runoff episode durations are broadly in agreement with previous estimates for lake filling and ponding of $\sim 10^2 - 10^4$ yr (Melas Chasma and Gale Crater; Williams & Weitz, 2014; Palucis et al., 2016, respectively). However, these younger lakes postdate the Noachian-Hesperian boundary and thus may not reflect similar climate conditions. The sparsity of well-preserved fluvial deposits in older, valley network-fed lake basins results in limited independent geological constraints on lake persistence to test our results. Nonetheless, estimates for total delta building timescales have been previously calculated for two valley network-fed basins: Eberswalde (a potential closed-basin lake) and Jezero (an open-basin lake). For Eberswalde, total delta-building runoff duration could have lasted $10^4 - 10^6$ yr (Moore et al., 2003; Irwin et al., 2015), with maybe a lake persisting for $> 10^5$ yr (Bhattacharya et al., 2005). Other studies have suggested total delta-building runoff durations as short as $10^1 - 10^2$ yr (Jerolmack et al., 2004; Lewis & Aharonson, 2006). For Jezero crater, total delta-building duration estimates have similarly ranged from $10^1 - 10^3$ yr (Fassett & Head, 2005; Salese et al., 2020; Lapôtre & Ielpi, 2020). However, because we do not know what fraction of a runoff episode is spent building a sedimentary deposit, these constraints are difficult to compare. Future insights into lake level persistence and variability, as captured by delta aggradation

and progradation, can hopefully be obtained as the Mars 2020 Perseverance rover explores Jezero crater, providing key independent constraints to test our results.

How do our episode duration estimates fit into the bigger picture of Mars' paleoclimate? Previous studies of valley network evolution suggest that early Mars was characterized by a long-lived runoff-producing climate lasting $> 10^5$ yr, assuming some intermittency frequency (Barnhart et al., 2009; Hoke et al., 2011). Our estimated durations suggest runoff production occurred in individual episodes lasting $10^2 - 10^5$ yr, separated by periods of water loss sufficiently long to reset the lake systems. As such, a large number of these individual runoff episodes likely comprised the total runoff-producing climate, interspersed by periods of negligible runoff. This is broadly consisent with mineralogical records suggesting wet climates were punctuated by long hyperarid intervals (Ehlmann & Edwards, 2014), as well as the presence of deeply incised inlet valleys that fed our paleolake database (Figure S2), implying multiple cycles of runoff and erosion (e.g., Rosenberg & Head, 2015; Luo et al., 2017). Ultimately, our lake-filling runoff episodes likely occurred during favorable climatic conditions associated with extremes of perhaps quasi-cyclical climate changes on Mars. Whether this cyclicity was modulated through astronomical variability (e.g., obliquity; Toon et al., 1980), geologically-derived fluctuations (e.g., redox oscillations; Wordsworth et al., 2021), or other driving forces, an intermittent climate forcing that can generate multiple runoff episodes lasting hundreds to thousands of years would be needed in order to reconcile with the Late Noachian / Early Hesperian hydrological record on Mars.

Acknowledgments

This work was supported by NASA MDAP grant 80NSSC17K0442. This is UT CPSH contribution #XXXXX. We are grateful to Alejandro Soto, Arihiro Kamada, Kathryn Steakley, Michael Mischna, and Robin Wordsworth for helpful discussions and access to climate model outputs. Datasets are available from Wordsworth et al. (2015), Steakley et al. (2019), Kamada et al. (2020), and Guzewich et al. (2021).

References

Armitage, J. J., Warner, N. H., Goddard, K., & Gupta, S. (2011). Timescales of alluvial fan development by precipitation on Mars. *Geophysical Research Letters*, *38*(17).

Barnhart, C. J., Howard, A. D., & Moore, J. M. (2009). Long-term precipitation and late-stage valley network formation: Landform simulations of Parana Basin, Mars. *Journal of Geophysical Research: Planets*, *114*(E1).

Benson, L. V., & Thompson, R. S. (1987). Lake-level variation in the Lahontan Basin for the past 50,000 years. *Quaternary Research*, *28*(1), 69–85.

Bhattacharya, J. P., Payenberg, T. H., Lang, S. C., & Bourke, M. (2005). Dynamic river channels suggest a long-lived Noachian crater lake on Mars. *Geophysical Research Letters*, *32*(10).

Bishop, J. L., Fairén, A. G., Michalski, J. R., Gago-Duport, L., Baker, L. L., Velbel, M. A., ... Rampe, E. B. (2018). Surface clay formation during short-term warmer and wetter conditions on a largely cold ancient Mars. *Nature Astronomy*, *2*(3), 206–213.

Buhler, P. B., Fassett, C. I., Head, J. W., & Lamb, M. P. (2014). Timescales of fluvial activity and intermittency in Milna Crater, Mars. *Icarus*, *241*, 130–147.

Cabrol, N. A., & Grin, E. A. (1999). Distribution, classification, and ages of Martian impact crater lakes. *Icarus*, *142*(1), 160–172.

Cabrol, N. A., & Grin, E. A. (2001). The evolution of lacustrine environments on Mars: Is Mars only hydrologically dormant? *Icarus*, *149*(2), 291–328.

Carr, M. H. (1987). Water on mars. *Nature*, *326*(6108), 30–35.

Christensen, P. R., Jakosky, B. M., Kieffer, H. H., Malin, M. C., McSween, H. Y., Nealson, K., ... others (2004). The thermal emission imaging system (THEMIS) for the Mars 2001 Odyssey Mission. *Space Science Reviews*, *110*(1-2), 85–130.

Craddock, R. A., & Howard, A. D. (2002). The case for rainfall on a warm, wet early Mars. *Journal of Geophysical Research: Planets*, *107*(E11), 21–1.

Edwards, C., Nowicki, K., Christensen, P., Hill, J., Gorelick, N., & Murray, K. (2011). Mosaicking of global planetary image datasets: 1. Techniques and data processing for Thermal Emission Imaging System (THEMIS) multi-spectral data. *Journal of Geophysical Research: Planets*, *116*(E10).

Ehlmann, B. L., & Edwards, C. S. (2014). Mineralogy of the Martian surface. *Annual Review of Earth and Planetary Sciences*, *42*.

Ehlmann, B. L., Mustard, J. F., Murchie, S. L., Bibring, J.-P., Meunier, A., Fraeman, A. A., & Langevin, Y. (2011). Subsurface water and clay mineral formation during the early history of Mars. *Nature*, *479*(7371), 53–60.

Fassett, C. I., & Head, J. W. (2005). Fluvial sedimentary deposits on Mars: Ancient deltas in a crater lake in the Nili Fossae region. *Geophysical Research Letters*, *32*(14).

Fassett, C. I., & Head, J. W. (2008). Valley network-fed, open-basin lakes on Mars: Distribution and implications for Noachian surface and subsurface hydrology. *Icarus*, *198*(1), 37–56.

Fastook, J. L., & Head, J. W. (2015). Glaciation in the Late Noachian Icy Highlands: Ice accumulation, distribution, flow rates, basal melting, and top-down melting rates and patterns. *Planetary and Space Science*, *106*, 82–98.

Goudge, T. A., Aureli, K. L., Head, J. W., Fassett, C. I., & Mustard, J. F. (2015). Classification and analysis of candidate impact crater-hosted closed-basin lakes on Mars. *Icarus*, *260*, 346–367.

Goudge, T. A., Fassett, C. I., Head, J. W., Mustard, J. F., & Aureli, K. L. (2016). Insights into surface runoff on early Mars from paleolake basin morphology and stratigraphy. *Geology*, *44*(6), 419–422.

Goudge, T. A., Fassett, C. I., & Mohrig, D. (2019). Incision of paleolake outlet canyons on Mars from overflow flooding. *Geology*, *47*(1), 7–10.

Grotzinger, J., Gupta, S., Malin, M., Rubin, D., Schieber, J., Siebach, K., ... others (2015). Deposition, exhumation, and paleoclimate of an ancient lake deposit, Gale crater, Mars. *Science*, *350*(6257).

Guzewich, S. D., Way, M., Aleinov, I., Wolf, E. T., Del Genio, A. D., Wordsworth, R. D., & Tsigaridis, K. (2021). 3D Simulations of the Early Martian Hydrological Cycle Mediated by a H2-CO2 Greenhouse. *Earth and Space Science Open Archive*, 47.

Hoke, M. R., Hynek, B. M., & Tucker, G. E. (2011). Formation timescales of large Martian valley networks. *Earth and Planetary Science Letters*, *312*(1-2), 1–12.

Horton, R. E. (1943). Hydrologic interrelations between lands and oceans. *Eos, Transactions American Geophysical Union*, *24*(2), 753–764.

Howard, A. D. (2007). Simulating the development of Martian highland landscapes through the interaction of impact cratering, fluvial erosion, and variable hydrologic forcing. *Geomorphology*, *91*, 332–363.

Irwin, R. P., Craddock, R. A., & Howard, A. D. (2005). Interior channels in Martian valley networks: Discharge and runoff production. *Geology*, *33*(6), 489–492.

Irwin, R. P., Lewis, K. W., Howard, A. D., & Grant, J. A. (2015). Paleohydrology of Eberswalde crater, Mars. *Geomorphology*, *240*, 83–101.

Jerolmack, D. J., Mohrig, D., Zuber, M. T., & Byrne, S. (2004). A minimum time for the formation of Holden Northeast fan, Mars. *Geophysical Research Letters*, *31*(21).

Kamada, A., Kuroda, T., Kasaba, Y., Terada, N., Nakagawa, H., & Toriumi, K. (2020). A coupled atmosphere–hydrosphere global climate model of early Mars: A 'cool and wet'scenario for the formation of water channels. *Icarus*, *338*, 113567.

Kite, E. S. (2019). Geologic constraints on early mars climate. *Space Science Reviews*, *215*(1), 10.

Kite, E. S., Lucas, A., & Fassett, C. I. (2013). Pacing early Mars river activity: Embedded craters in the Aeolis Dorsa region imply river activity spanned (1–20) Myr. *Icarus*, *225*(1), 850–855.

Kleinhans, M. G., van de Kasteele, H. E., & Hauber, E. (2010). Palaeoflow reconstruction from fan delta morphology on Mars. *Earth and Planetary Science Letters*, *294*(3-4), 378–392.

Lapôtre, M. G., & Ielpi, A. (2020). The pace of fluvial meanders on Mars and implications for the western delta deposits of Jezero crater. *AGU Advances*, *1*(2), e2019AV000141.

Lewis, K. W., & Aharonson, O. (2006). Stratigraphic analysis of the distributary fan in Eberswalde crater using stereo imagery. *Journal of Geophysical Research: Planets*, *111*(E6).

Luo, W., Cang, X., & Howard, A. D. (2017). New Martian valley network volume estimate consistent with ancient ocean and warm and wet climate. *Nature Communications*, *8*, 15766.

Malin, M. C., & Edgett, K. S. (2000). Sedimentary rocks of early Mars. *Science*, *290*(5498), 1927–1937.

Mangold, N., Ansan, V., Masson, P., & Vincendon, C. (2009). Estimate of aeolian dust

thickness in Arabia Terra, Mars: Implications of a thick mantle (> 20 m) for hydrogen detection. *Géomorphologie: relief, processus, environnement*, *15*(1), 23–32.

Matsubara, Y., Howard, A. D., & Drummond, S. A. (2011). Hydrology of early Mars: Lake basins. *Journal of Geophysical Research: Planets*, *116*(E4).

Mischna, M. A., Richardson, M. I., Wilson, R. J., & McCleese, D. J. (2003). On the orbital forcing of Martian water and CO2 cycles: A general circulation model study with simplified volatile schemes. *Journal of Geophysical Research: Planets*, *108*(E6).

Moore, J. M., Howard, A. D., Dietrich, W. E., & Schenk, P. M. (2003). Martian layered fluvial deposits: Implications for Noachian climate scenarios. *Geophysical Research Letters*, *30*(24).

Palucis, M. C., Dietrich, W. E., Williams, R. M., Hayes, A. G., Parker, T., Sumner, D. Y., ... Newsom, H. (2016). Sequence and relative timing of large lakes in Gale crater (Mars) after the formation of Mount Sharp. *Journal of Geophysical Research: Planets*, *121*(3), 472–496.

Palumbo, A. M., & Head, J. W. (2018). Early Mars Climate History: Characterizing a "Warm and Wet" Martian Climate With a 3-D Global Climate Model and Testing Geological Predictions. *Geophysical Research Letters*, *45*(19), 10–249.

Palumbo, A. M., Head, J. W., & Wordsworth, R. D. (2018). Late Noachian Icy Highlands climate model: Exploring the possibility of transient melting and fluvial/lacustrine activity through peak annual and seasonal temperatures. *Icarus*, *300*, 261–286.

Ramirez, R. M., Craddock, R. A., & Usui, T. (2020). Climate simulations of early Mars with estimated precipitation, runoff, and erosion rates. *Journal of Geophysical Research: Planets*, *125*(3), e2019JE006160.

Rosenberg, E. N., & Head, J. W. (2015). Late Noachian fluvial erosion on Mars: Cumulative water volumes required to carve the valley networks and grain size of bed-sediment. *Planetary and Space Science*, *117*, 429–435.

Salese, F., Kleinhans, M. G., Mangold, N., Ansan, V., McMahon, W., de Haas, T., & Dromart, G. (2020). Estimated Minimum Life Span of the Jezero Fluvial Delta (Mars). *Astrobiology*, *20*(8), 977–993.

Scanlon, K., Head, J., & Wordsworth, R. D. (2016). Snowmelt rates in modeled early Mars climate scenarios. In *Lunar and planetary science conference* (p. 1532).

Scanlon, K. E., Head, J. W., Madeleine, J.-B., Wordsworth, R. D., & Forget, F. (2013). Orographic precipitation in valley network headwaters: Constraints on the ancient

Martian atmosphere. *Geophysical Research Letters*, *40*(16), 4182–4187.

Schon, S. C., Head, J. W., & Fassett, C. I. (2012). An overfilled lacustrine system and progradational delta in Jezero crater, Mars: Implications for Noachian climate. *Planetary and Space Science*, *67*(1), 28–45.

Smith, D. E., Zuber, M. T., Frey, H. V., Garvin, J. B., Head, J. W., Muhleman, D. O., ... others (2001). Mars Orbiter Laser Altimeter: Experiment summary after the first year of global mapping of Mars. *Journal of Geophysical Research: Planets*, *106*(E10), 23689–23722.

Soto, A., Richardson, M., & Newman, C. (2010). Global constraints on rainfall on ancient Mars: Oceans, lakes, and valley networks. In *Lunar and Planetary Science Conference, Abstract no. 1533* (p. 2397).

Steakley, K., Murphy, J., Kahre, M., Haberle, R., & Kling, A. (2019). Testing the impact heating hypothesis for early Mars with a 3-D global climate model. *Icarus*, *330*, 169–188.

Stucky de Quay, G., Goudge, T. A., & Fassett, C. I. (2020). Precipitation and aridity constraints from paleolakes on early Mars. *Geology*, *48*(12), 1189–1193.

Toon, O. B., Pollack, J. B., Ward, W., Burns, J. A., & Bilski, K. (1980). The astronomical theory of climatic change on Mars. *Icarus*, *44*(3), 552–607.

Turbet, M., Gillmann, C., Forget, F., Baudin, B., Palumbo, A., Head, J., & Karatekin, O. (2020). The environmental effects of very large bolide impacts on early Mars explored with a hierarchy of numerical models. *Icarus*, *335*, 113419.

Urata, R. A., & Toon, O. B. (2013). Simulations of the martian hydrologic cycle with a general circulation model: Implications for the ancient martian climate. *Icarus*, *226*(1), 229–250.

von Paris, P., Petau, A., Grenfell, J., Hauber, E., Breuer, D., Jaumann, R., ... Tirsch, D. (2015). Estimating precipitation on early Mars using a radiative-convective model of the atmosphere and comparison with inferred runoff from geomorphology. *Planetary and Space Science*, *105*, 133–147.

Williams, R. M., & Weitz, C. M. (2014). Reconstructing the aqueous history within the southwestern Melas basin, Mars: Clues from stratigraphic and morphometric analyses of fans. *Icarus*, *242*, 19–37.

Wordsworth, R. D. (2016). The climate of early Mars. *Annual Review of Earth and Planetary Sciences*, *44*, 381–408.

Wordsworth, R. D., Forget, F., Millour, E., Head, J., Madeleine, J.-B., & Charnay, B. (2013). Global modelling of the early martian climate under a denser CO2 atmosphere: Water cycle and ice evolution. *Icarus*, *222*(1), 1–19.

Wordsworth, R. D., Kerber, L., Pierrehumbert, R. T., Forget, F., & Head, J. W. (2015). Comparison of "warm and wet" and "cold and icy" scenarios for early Mars in a 3-D climate model. *Journal of Geophysical Research: Planets*, *120*(6), 1201–1219.

Wordsworth, R. D., Knoll, A. H., Hurowitz, J., Baum, M., Ehlmann, B. L., Head, J. W., & Steakley, K. (2021). A coupled model of episodic warming, oxidation and geochemical transitions on early Mars. *Nature Geoscience*, *14*(3), 127–132.

Supporting Information for "Limits on runoff episode duration for early Mars: integrating climate models and lake hydrology"

Gaia Stucky de Quay[1,2], Timothy A. Goudge[1,2], Edwin S. Kite[3], Caleb I. Fassett[4], and Scott D. Guzewich[5]

[1]Jackson School of Geosciences, University of Texas at Austin, Austin, Texas 78712, USA

[2]Center for Planetary Systems Habitability, University of Texas at Austin, Austin, Texas 78712, USA

[3]Department of the Geophysical Sciences, University of Chicago, Chicago, Illinois 60637, USA

[4]NASA Marshall Space Flight Center, Huntsville, Alabama 35805, USA

[5]NASA Goddard Space Flight Center, Greenbelt, Maryland 20771, USA

Corresponding author: G. Stucky de Quay, (g.stucky@utexas.edu)

March 25, 2021, 4:20pm

Contents of this file

Introduction

This Supporting Information (SI) document contains additional information on assumptions made during mapping of open- and closed-basin lakes (Text S1). It also describes the effects of sedimentary infill on our results (Text S2). Then, it provides a full derivation of the volumetric and timescale functions presented in equations (2) – (4) in the main text (Text S3). Further, the SI contains a schematic overview of the early Mars climate and the relevant parameters used in this study (Figure S1), maps of the coupled lake systems (Figure S2), as well as modified results from Figure 4 assuming a climate regime with no evaporation (Figure S3) and modified results if we reduce the population of coupled systems following Text S1 (Figures S4 and S5). Finally, the SI provides four tables (Tables S1-S4): Table S1 lists additional information for studies shown in Figure 1, Table S2 summarizes data that are available for 8 studies (4 geomoprhic analyses + 4 climate models), Table S3 presents our full database of coupled lake systems and their morphometric parameters, and Table S4 summarizes the climate model scenarios used for Figure 4 (and Figures S3,S5).

Text S1. Identification of open- vs. closed-basin lakes

Open- and closed- basin lakes were classified based on whether or not they contained an outlet canyon. Although it is possible some overflow may have occurred without visible outlet canyon erosion, we interpret the lack of geologic evidence for overflow as an indication that the lake system was closed (Supplementary Figure S2). However, because the craters we interpret as closed basins may have been modified by later processes, the lack of an observed outlet is not definitive proof that one never formed. Based on contextual evidence, however, the odds that more than 1-2 of the basins we interpret as closed overflowed is low. Further, the observation that closed-basin lakes always allow greater water inputs (smaller areas, larger basins) than their coupled open-basin lake counterparts is in line with the assumption that they were not breached.

Stucky de Quay et al. (2020) showed that removal of closed-basin lakes with depressions on their rims (potential outflows that did not form defined canyons) did not affect distributions of hydrologic reconstructions. Here we apply a similar modification to our results and remove two systems from our analyses that could arguably be of reduced confidence: Basin IDs 47/13 and 231/216 (see Supplementary Table S3; Figure S2). Recalculation of results using the 5 remaining coupled systems (as shown originally in Figures 2e,f and 4 in the main text) are shown in Supplementary Figures S4 and S5. These results show that the removed basins lie within the range of our original population, and thus do not affect our overarching quantitative findings: the range of T_{max}/T_B values in Figures 2e,f ($1.6 - 63$) or the range of episode runoff durations in Figure 4 ($10^2 - 10^5$ yr).

Text S2. Basin infill and sedimentary volume considerations

Here we consider various infilling scenarios—depending on when they occur—and how they may (or may not) affect our results.

First, although the morphology of basins indicates they have been significantly infilled (e.g., flat crater floors in Figure 2a and Figures S2a-f), the majority of this infill would have occurred prior to the valley network era (i.e., during the Noachian period; Malin & Edgett, 2000; Craddock et al., 2002). As such, this infill occurred before our valley network-fed runoff events and do not affect our results. Subsequently, during the valley network period, sediment may also have been eroded from the valley network watersheds (from both open- and closed-basin lakes) and deposited into the basins for any episode preceding the breaching runoff episode (e.g., any of the episodes before breaching episode in Figure S1a indicated by (i)). This sediment volume would not affect our results because it was deposited prior to the breaching episode, and our measured lake volumes exclude this sediment volume.

Second, sediment may be added to the basins during the breaching runoff episode (breaching episode in Figure S1a, (ii)). This sediment could be derived from either inlet incision (from both open- and/or closed basin lake watersheds) and/or outlet canyon incision (deposited in the downstream closed-basin lake). In both cases, this sedimentary infill will not affect our results because we are only concerned with basin water volumes at the end of runoff episode. In other words, any sediment volume that is eroded, transported, and deposited in the basin at any point within the breaching runoff episode *remains* in the basin up to the present—thus, when we measure lake volumes using present-day topography, the sediment volumes are not incorporated in our lake volumes. In this

way, our lake volumes consider only the water volume and are not affected by synfluvial sedimentation during the breaching episode.

Third, infill may occur after the breaching runoff episode. This could either be due to (a) subsequent runoff episodes (i.e., if there are many more runoff episodes after the breaching episode; Figure S1a, (iii)), or (b) postfluvial processes such as aeolian deposition. Although these would have an impact on our results, they are unlikely to significantly modify our volume estimates, as we explain below. To assess the maximum value of the first contribution, let us make the assumption that the breaching episode is the very first runoff episode to occur in a series of episodes (e.g., the breaching episode is the first peak in Figure S1a). This would mean that approximately the entire eroded watershed volume (measured from the inlets) would be deposited into the basin after our breaching event, resulting in our measured lake volumes being an underestimate. For Jezero crater, the eroded volume from the watershed is $\sim$58 km^3 (Fassett and Head, 2005). The basin volume is $\sim$424 km^3 (see Open Basin ID 45 from Stucky de Quay et al., 2020). This would mean the basin volume before sediment deposition from inlets would have been 482 km^3, i.e., only 14% greater. For the second contribution, aeolian deposits are likely to be a few tens of meters (e.g., dust mantle thickness of $\sim$20 m from Mangold et al., 2009) and would only infill $\sim$10% of the basins, which are on average $\sim$200 m deep (Stucky de Quay et al., 2020). As such, even if we sum up both liberal contributions, paleolake volumes could only have been up to $\sim$24% larger, which would change episode duration values by the same proportion, and thus not significantly alter our results.

In summary, sediment deposition into the basins occurring before or during the breaching runoff episode does not affect our lake volume calculations, and sediment deposition

occurring after the breaching runoff episode (whether through fluvial or aeolian processes) is not significant relative to the size of the basin.

Text S3. Full derivation of lake hydrology and timescale expressions

Open-basin lake. In an embedded lake system, where an open-basin lake is located within the watershed of a closed-basin lake, the changes in lake volume over time can be calculated using a simple model. The following derivation of this expression builds on the standard hydrological balance in equation (1) to derive the final expression for lake volumes in equations (2) and (3) in the main text.

For an open-basin lake (O), the volume of water, v_O within its basin as a function of time, t, before breaching (and excluding any losses; discussed further later) can be expressed as

$$v_O[t \leq T_B] = (A_{L,O} + A_{W,O})P \times t, \tag{6}$$

assuming a steady precipitation rate, P, across the lake area, $A_{L,O}$ and watershed area $A_{W,O}$. When the volume of water within open-basin lake reaches the maximum volume held by the basin, i.e., $v_O = V_{L,O}$, then the lake breaches. When this event occurs at a time $t = T_B$, the lake overflows and causes catastrophic canyon erosion (Fassett & Head, 2008; Goudge et al., 2019). Due to the lowered outlet canyon floor, some water drains from the open-basin lake into the downstream closed basin lake. The remaining volume of water in the basin contained after breaching is given by V_R. Since the open- and closed-basin lakes are now hydrologically connected—and the open-basin lake volume remains steady at V_R—any additional water input to this volume is not topographically contained and would be transferred downstream. We can now express these two time-dependent states as a piece-wise function:

$$v_O = \begin{cases} (A_{L,O} + A_{W,O})Pt & \text{if } t \leq T_B; \\ V_R & \text{if } t > T_B; \end{cases} \tag{7}$$

This function describes how the lake volume changes as a function of t, given the measured morphometric parameters $A_{L,O}$, $A_{W,O}$, and V_R, and a known P. Below we derive a similar, expression for the closed-basin lake.

Closed-basin lake. For a closed-basin lake (C) in an embedded coupled system, the changes in lake volume can also be broken down into before and after open-basin lake breaching. Before the breach at T_B, the closed-basin lake is not connected to the upstream open-basin lake, and so the volume of water that accumulates in the basin, again excluding losses, is simply proportional to the combined watershed and lake areas, analogous to equation (6):

$$v_C[t \leq T_B] = (A_{L,C} + A_{W,C})P \times t. \tag{8}$$

However, after the open-basin lake breach two key events occur. First, the drained volume in the upstream open-basin lake is transferred to the closed-basin lake; we assume this to be instantaneous following a catastrophic erosion event (Goudge et al., 2019). Second, the closed-basin system has now captured the watershed of the upstream open-basin lake, such that the contributing watershed now consists of both watersheds. This means that the volume of a closed-basin after T_B consists of three terms: (i) the total volume accumulated from equation (8) up to the breach, $(A_{L,C} + AW, C)PT_B$, (ii) the transferred water volume from upstream lake overflow and outlet canyon erosion, $V_{L,O} - V_R$, and (iii) the new rate of volume accumulation from the combined watersheds after breaching, $(A_{L,O} + A_{W,O} + A_{L,C} + A_{W,C})P(t - T_B)$. We can thus express the post-breach volume of a closed-basin lake as the total sum of these terms, such that

$$v_C[t > T_B] = (A_C P T_B) + (V_{L,O} - V_R) + (A_{L,O} + A_{W,O} + A_{L,C} + A_{W,C})P(t - T_B). \tag{9}$$

By expanding the third term and canceling out repeated terms, equation (9) can be written as

$$v_C[t > T_B] = V_{L,O} - V_R + (A_{L,O} + A_{W,O} + A_{L,C} + A_{W,C})Pt - (A_{L,O} + A_{W,O})PT_B. \quad (10)$$

In order to simplify this, we substitute the term for the open-basin lake volume at T_B. The open-basin lake volume v_O is equal to $V_{L,O}$ when $t = T_B$. Hence, we can rewrite equation (6) as

$$V_{L,O} = (A_{L,O} + A_{W,O})PT_B. \quad (11)$$

Since this is equivalent to the final term in equation (10), we substitute equation (11) into equation (10), which, after simplifying, results in

$$v_C[t > T_B] = (A_{L,O} + A_{W,O} + A_{L,C} + A_{W,C})Pt - V_R. \quad (12)$$

Similarly to equation (7), we express the volume of a closed-basin lake as a function of time, using piece-wise functions built from equation (8) and (12):

$$v_C = \begin{cases} (A_{L,C} + A_{W,C})Pt & \text{if } t \leq T_B; \\ (A_{L,O} + A_{W,O} + A_{L,C} + A_{W,C})Pt - V_R & \text{if } t > T_B; \end{cases} \quad (13)$$

As a result, we now have two sets of equations, (7) and (13), which describe open- and closed-basin lake volumes, respectively, as a function of time, both before and after open-basin lake breaching. However, both of these expressions require knowledge of a precipitation rate, P. Since both open- and closed-basin lakes are spatially coincident, and thus it is safe to assume they experience the same precipitation rate, we can remove the precipitation term by normalizing both expressions, obtaining lake volume expressions as a function of relative time (see below).

Normalization. In order to solve for lake volumes as a function of relative time, we remove the P dependency from equations (7) and (13). To do this, we can take equation (11), which defines the open-basin lake volume at the time of breach, and rearrange it so that we instead obtain a definition for P:

$$P = \frac{V_{L,O}}{(A_{L,O} + A_{W,O})T_B}. \tag{14}$$

Since the precipitation rate is assumed to be the same for both open- and closed-basin lakes, we substitute equation (14) into the precipitation term in equations (7) and (13). This means that Pt can now be expressed as $\frac{V_{L,O}}{A_{L,O}+A_{W,O}}\left(\frac{t}{T_B}\right)$; this allows the volume expressions to be a function of time relative to breaching, i.e., $v = f\left(\frac{t}{T_B}\right)$. This substitution results in the following expressions:

$$v_O = \begin{cases} V_{L,O}\left(\dfrac{t}{T_B}\right) & \text{if } t \leq T_B; \\ V_R & \text{if } t > T_B; \end{cases} \tag{15}$$

$$v_C = \begin{cases} (A_{L,C} + A_{W,C})\dfrac{V_{L,O}}{A_{L,O} + A_{W,O}}\left(\dfrac{t}{T_B}\right) & \text{if } t \leq T_B; \\ (A_{W,O} + A_{L,O} + A_{L,C} + A_{W,C})\dfrac{V_{L,O}}{A_{L,O} + A_{W,O}}\left(\dfrac{t}{T_B}\right) - V_R & \text{if } t > T_B. \end{cases} \tag{16}$$

Note that the volume expressions are essentially normalized to the morphology of the open-basin lake. Equations (15) and (16) are similar to equations (2) and (3) in the main text, but do not take into account losses due to evaporation, for which our approach is described below.

Evaporation losses. Thus far, equations (6)-(16) do not consider the effects of evaporation on lake volumes. Equation (1) in the main texts shows that evaporation is assumed to occur over the lake area. Note that we assume here all precipitation from the water-

shed ends up in the lake, whether through surface runoff or infiltration and subsequent re-emergence into the valleys or the lake. Stucky de Quay et al. (2020) investigated how losses from the watershed affected the water balance, showing that even a 50% fractional loss (where half of the precipitation incident on the watershed is lost) results in limited changes to the overall hydrological reconstruction of the lake system. As such, the only lake loss explicitly considered in this study is evaporation from the lake surface.

In order to take into account losses due to lake evaporation, we can express evaporation as a fraction of the precipitation. One way to do this is using the aridity index, AI, which is simply the ratio of precipitation to evaporation ($\mathrm{AI} = P/E$). Another, related term, is the X ratio defined in Howard (2007), which is given as $X = (E - P)/P$, if we assume that all the precipitation ends up in the lake as described above. Note that both values are interchangeable, as $X = 1/\mathrm{AI} - 1$. The aridity index benefits from being a common parameter that can be easily compared to terrestrial values; however, the X ratio results in a more simplified balance expression. For instance, when using the aridity index as a substitute for the evaporative term, equation (1) becomes

$$V_L = ((A_W + A_L)P - (A_L)\frac{P}{\mathrm{AI}})T, \tag{17}$$

whereas the same equation expressed using the X ratio would take the form

$$V_L = (A_W - XA_L)PT. \tag{18}$$

Due to the simplicity of equation (18) relative to equation (17), we favor the X ratio for display purposes. In a system with no evaporation, the aridity index is infinite, and the X ratio is -1. For this study we use a semiarid scenario as proposed in Stucky de Quay et al., (2020), where open-basin lakes need a minimum global aridity index $\mathrm{AI} \simeq 0.26$ to

overflow (consistent with the semiarid hydrological regime required by Matsubara et al., 2011). This value is the most arid scenario that allows all open-basin lakes on Mars to exist. Timescale results in Figure 3b, Figure 4, and Figure S1, consider two end-member scenarios: no evaporation and AI = 0.26. Adding the evaporative terms in equation (18) to equations (15) and (16) results in the final equations (2) and (3) in the main text. Finally, to calculate the values plotted in Figures 3b,c, we normalize equations (2) and (3) by the volume of the closed-basin lake, i.e., both sides of both equations are divided by $V_{L,C}$. This allows all the plots to have maximum permitted normalized volumes < 1.

Embedded vs. Adjacent systems. The expressions derived thus far are only applicable to embedded coupled systems, i.e., systems wherein some lake overflow volume from the open-basin lake is transferred directly (and instantaneously) to the closed-basin lake, and where the closed-basin lake captures the watershed of the open-basin lake. However, one out of our seven mapped coupled systems is not embedded (Table S1), and is instead classified as an adjacent coupled system. These systems share significant drainage divides and are also assumed to be formed synchronously, with the main difference to embedded systems being that the outlet canyon does not flow into the closed-basin lake. For the case of our one adjacent system, $v_O = f(t/T_B)$ remains the same, but equation (3) takes the simpler, modified form:

$$v_C = (A_{W,C} - XA_{L,C})\frac{V_{L,O}}{A_{W,O} - XA_{L,O}}\left(\frac{t}{T_B}\right), \tag{19}$$

for all values of $\frac{t}{T_B}$ (i.e., independent of breaching), and where $v_C < V_{L,C}$. For our unique coupled system (Basin ID 171/140; Table S1), we use equation (19) instead of (3). Note that Figure 3b,c only includes the 6 embedded systems, and not the adjacent system,

since it does not follow the schematic behavior presented in Figure 3a.

Timescales. In addition to investigating lake volumes change with respect to relative timescales, we also derive expressions to solve for the absolute runoff episode duration lengths permitted. By rearranging equation (14), we can obtain an expression for T_B, such that

$$T_B = \frac{V_{L,O}}{(A_{L,O} + A_{W,O})P}. \tag{20}$$

Since the breaching timescale is the minimum timescale permitted to allow for the open-basin lake to breach, T_B, we combine this with the evaporation loss term in equation (18) to obtain the equation (4) presented in the main text. Conversely, for the maximum timescale for an embedded couple system, we take equation (12) and find the maximum volume permitted, $v_C = V_{L,C}$, and set $t = T_{max}$, such that

$$V_{L,C} = (A_{L,O} + A_{W,O} + A_{L,C} + A_{W,C})PT_{max} - V_R. \tag{21}$$

We then use the same evaporation expression from equation (18), and rearrange to solve for T_{max}, resulting in equation (5) in the main text. For our adjacent coupled system, equation (21) takes the simpler form:

$$V_{L,C} = (A_{L,C} + A_{W,C})PT_{max}, \tag{22}$$

as it has no dependency on the open-basin lake morphology. Accounting for evaporative losses, this results in the following expression for T_{max} as recorded by adjacent coupled systems:

$$T_{max} = \frac{V_{L,C}}{(A_{W,C} - XA_{L,C})P}, \tag{23}$$

analogous to equation (5) in the main text.

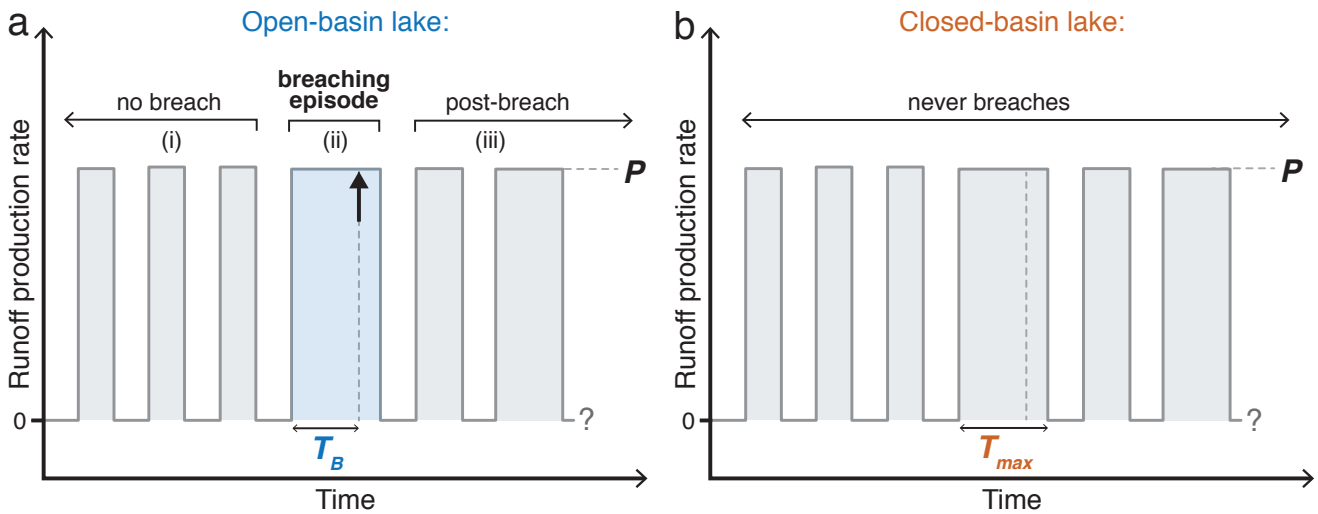

Figure S1. Schematic oscillating climate for late Noachian / early Hesperian Mars (>3.7 Ga), with variable runoff production rate over time (modified from Figure S1 in Stucky de Quay et al., 2020). Note that episodic runoff may be sourced from rainfall or snowmelt (e.g., Kite et al., 2013; Kite, 2019). In a coupled lake system, the (a) open-basin lake breaches (= black arrow) if a given runoff episode is sufficiently continuous, i.e., the duration exceeds T_B, and enough liquid water is supplied (where P is the time-averaged runoff rate). We term this episode the 'breaching runoff episode' (= light blue shaded box; (ii)). However, within the same coupled system, the (b) closed-basin lake never breaches. Thus, we can estimate maximum runoff episode duration, T_{max}, for a given runoff rate, P, from climate model outputs. In this work we quantify T_B and T_{max} for the breaching runoff episode of each coupled system. Importantly, episode durations before the breaching episode (see (i)) must always be less than T_B, but can be longer or shorter after the breaching episode (see (iii)). No episode duration can ever be greater than T_{max} (as this would cause the closed-basin lake to breach). Note that to erode the deep valley networks which feed these coupled systems, water volumes greatly exceeding lake volumes are required, suggesting multiple runoff events likely occurred (see Discussion section in the main text).

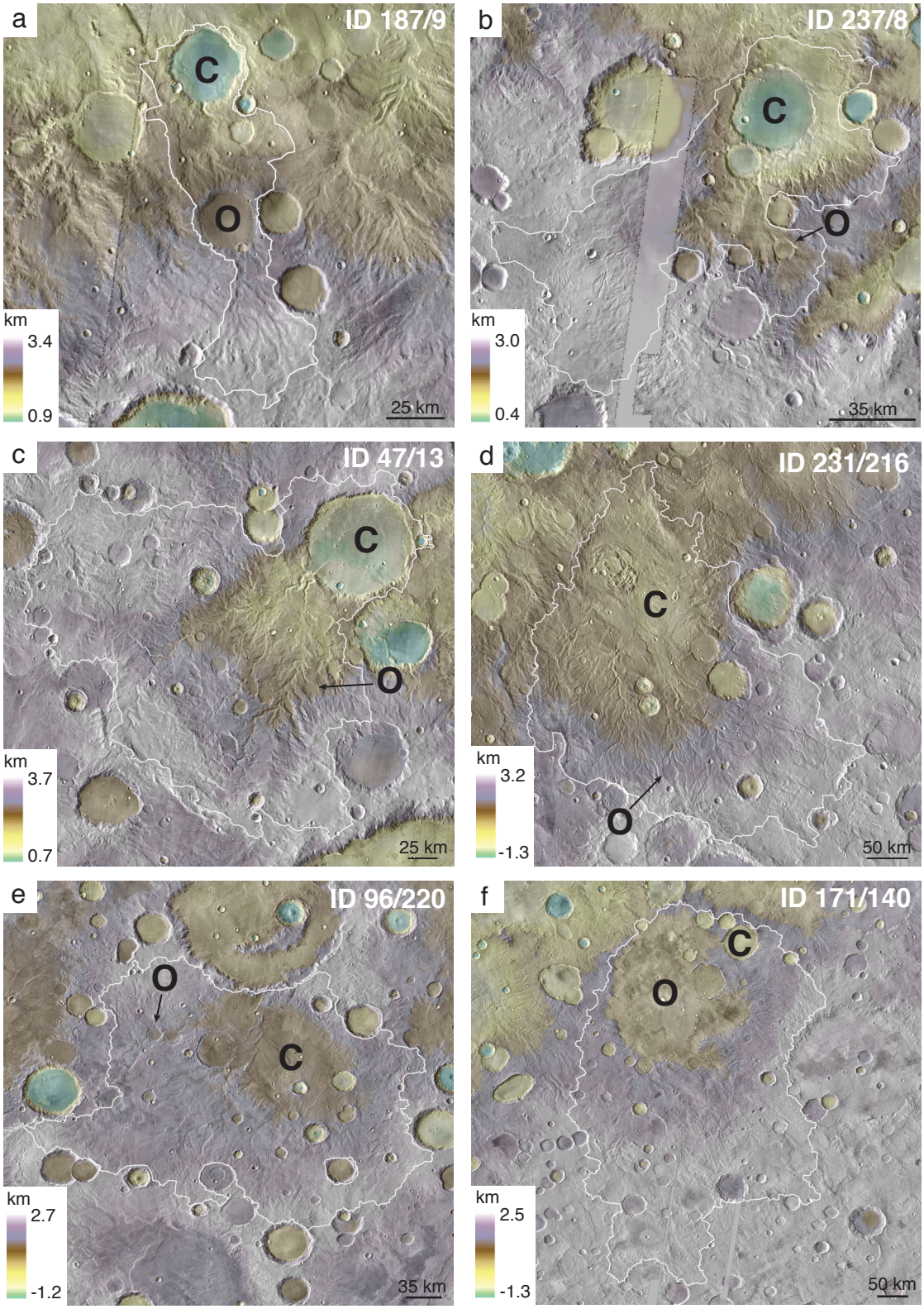

Figure S2. Coupled lake systems identified on Mars (excluding ID 185/89 in Figure 2a). O = open-basin lake; C = closed basin lake; white polygon = combined watershed and lake areas of each coupled system (Table S3). Elevation and images from MOLA and THEMIS, respectively.

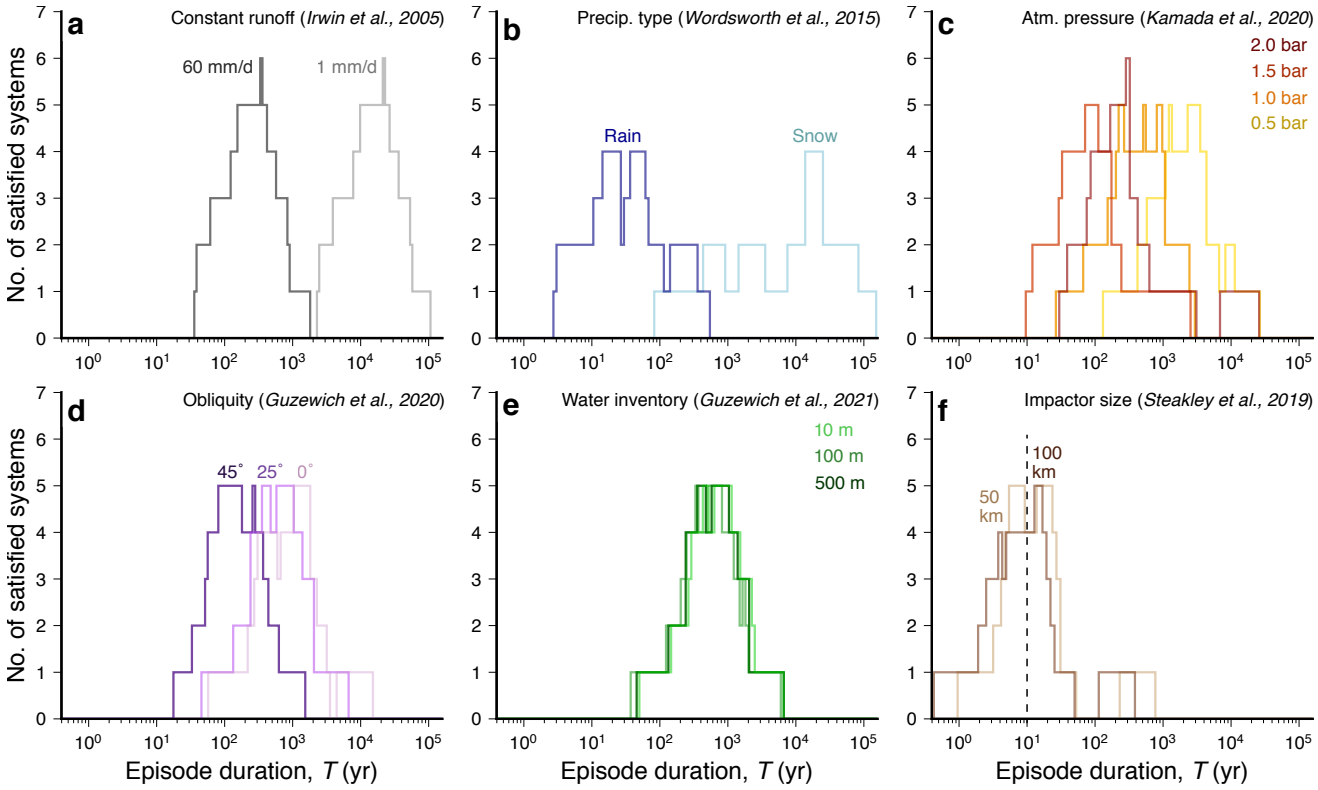

Figure S3. Distribution of runoff episode durations (assuming no evaporation; E=0) that satisfy the 7 studied coupled systems using different runoff constraints. See Figure 4 in main text for comparison and further details (where aridity index, AI = 0.26).

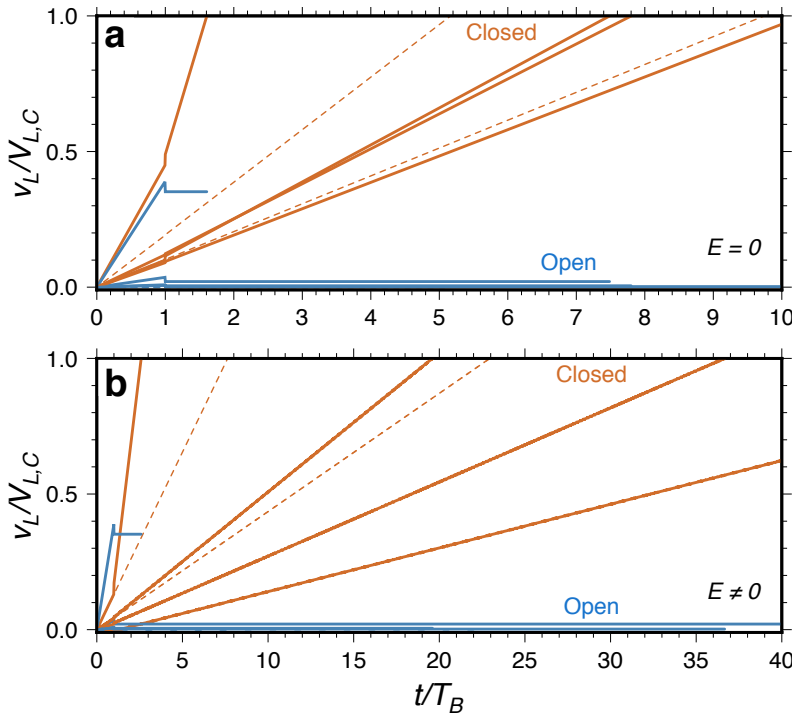

Figure S4. Lake volume changes over time (analogous to Figure 2e,f), but excluding two systems: Basin IDs 47/13 and 231/216 (shown in dashed lines; see Supplementary Text S1 for discussion; Table S3; Figure S2). Note that the total range of T_{max}/T_B remains unchanged. See Figures 2e,f for additional details.

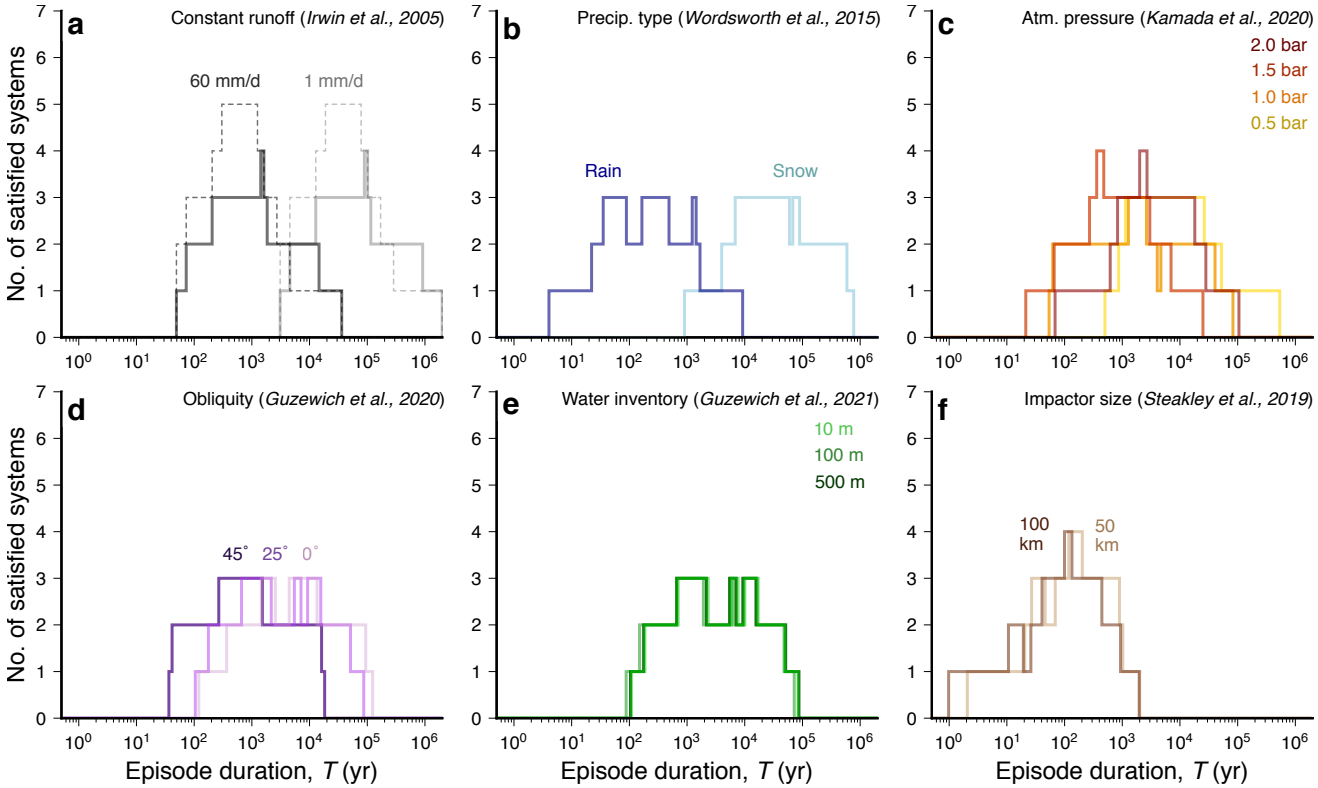

Figure S5. Distribution of runoff episode durations that satisfy 5 of the studied coupled systems using different runoff constraints. Here we exclude two systems: Basin IDs 47/13 and 231/216 (see Supplementary Text S1 for discussion; Table S3; Figure S2). Note that the new maximum is now 5. Dashed distributions in (a) show original distributions from Figure 4 for comparison. See Figure 4 in main text for further details (where all 7 coupled systems are considered). Note that location of peaks is similar to Figure 4.

Table S1. Water availability rates and their data sources. Minimum and/or maximum values are shown below in the format they were published in (before converted to an order of magnitude estimate in mm per Earth year for Figure 1 in the main text). Rates/studies are listed in the same order as Figure 1. When min/max results were not explicitly stated or tabulated, these were estimated from scale bar ranges provided in figures. Specific location of data in the original publication is indicated in the final column. For the models where the xy-data was made available (indicated with an asterisk), or geological runoff constraints where all results were tabulated and provided, we also present those results in Table S3.

Rate	Study	Data location
$8 - 3000$ m in 10^6 yr	Fastook et al. (2015)	Table 1; Figs. 7-12 (b,f,j)
$-2 - 0.5$ $\log_{10}$(kg/m^2/avg.) in 5 years	Wordsworth et al. (2015)*	Fig. 5a
$0.009 - 1.26$ cm/yr	Urata et al. (2013)	Table 4
$0 - 33$ kg/m^2 in 40 years	Wordsworth et al. (2013)	Figs. 4, 6, 7, 10
$0 - 3$ $\log_{10}$ of mm/yr	Kamada et al., (2020)*	Fig. 8
$0.001 - 1$ mm/day	Von Paris et al., (2015)	Abstract/Fig. 8
$< 10^-4 - 10^-2$ mm/hr	Scanlon et al. (2013)	Section 3.1
$0 - 40$ mm in a year	Palumbo et al. (2018)	Section 3.3.2/Fig. 11
$-1 - 0.5$ $\log_{10}$(m/yr/avg.)	Wordsworth et al. (2015)*	Fig. 4b
$30mm - 2.4$ m in a year	Ramirez et al. 2020	Figs. 11,12
< 100 mm/yr	Guzewich et al. (2020)*	Fig. 2
$1.5 - 10.6$ mm/day	Von Paris et al. (2015)	Table 1/Section 2.2.3
$0.7 - 9.69$ mm/day	Ramirez et al. (2020)	Table 1
$0.23 - 5.84$ m in one year	Steakley et al. (2020)*	Abstract
$0.1 - 6$ cm/day	Irwin et al. (2005)	Table 1
< 100 cm/yr	Soto et al. (2010)	Fig. 1B
$0.001 - 5$ cm in a southern winter	Mischna et al. (2003)	Figs. 6, 8, 10
$0.4 - 63$ cm/d	Hoke et al. (2011)	Table 3
< 0.14 m/day	Scanlon et al. (2016)	Section 3.1
$< 2 - 3$ mm/hr	Kite et al., (2013)	Section 8.5

Table S2. Precipitation/runoff constraints on early Mars from select previous studies. Figure 1 in the main text and Table S1 provide an order of magnitude overview of various studies (n=21), but here we provide additional details for 8 studies for which the data were made available to the authors. Rates from each study are expressed as the logarithmic mean and standard deviation ($\mu^{+\sigma}_{-\sigma}$) of provided datapoints[a]. The last column lists the number of runoff/precipitation datapoints from each study, as well as the percent of area of Mars that is covered.

Rate (mm/yr)	Type	Study	Data points (coverage)[a]
Local geological constraints:			
2378^{+4806}_{-1591}	Peak runoff	Irwin et al. (2005)	15 (0.7%)
6472^{+9850}_{3906}	Peak runoff	Hoke et al. (2011)	7 (0.5%)
1394^{+1185}_{-641}	Runoff	Von Paris et al. (2015)	18 (<0.1%)
848^{+1217}_{-500}	Runoff	Ramirez et al. (2020)	8 (0.1%)
Global climate models:			
81^{+1067}_{-75}	Rainfall	Wordsworth et al. (2015)	2185
$800^{+587}_{-339}; 3582^{+8300}_{-2502}$	Precipitation	Steakley et al (2020)[b]	2100
$10^{+12}_{-5}; 40^{+61}_{-24}$	Precipitation	Guzewich et al. (2020)[b]	3312
$3^{+4}_{-2}; 46^{+494}_{-42}$	Precipitation	Kamada et al. (2020)[b]	2048

[a] For global climate models, spatial coverage ∼100%, and datapoints correspond to the number of data nodes in each model grid. [b] For models that consider more than one climate scenario, we provide both minimum and maximum runoff scenarios.

Table S3. List of 7 coupled lake systems on Mars used for this study (originally identified in Stucky de Quay et al., 2020). Each row corresponds to a single coupled system, providing details on both the open- and closed-basin lake morphological parameters. The system type indicates whether it as an embedded (E) or adjacent (A) system (see main text for description).

Open-basin lakes (O)							Closed-basin lakes (C)						Type
Basin ID	Lat. (°)	Long. (°)	Lake Area, $A_{L,O}$ (m^2)	Lake Volume, $V_{L,O}$ (m^3)	Watershed Area, $A_{W,O}$ (m^2)	Remaining Lake Volume, V_R (m^3)	Basin ID	Lat. (°)	Long. (°)	Lake Area, $A_{L,C}$ (m^2)	Lake Volume, $V_{L,C}$ (m^3)	Watershed Area, $A_{W,C}$ (m^2)	
187	-7.2	43.0	672583920	70758474568	2693891297	63762980452	9	-5.8	42.8	937334813	181170078070	2951851160	E
[a]231	7.8	47.8	71349069	2214100227	922578879	1213230624	216	11.2	47.3	16423192980	1999070439438	74750868307	E
185	2.2	45.5	153020661	12052978646	1347895789	6879905806	89	3.0	45.5	1195725678	331637791895	2933305480	E
237	-4.4	88.4	42189599	3528718923	835736020	2054182263	8	-3.3	88.3	2159319657	393910203622	9585477072	E
[a]47	-10.4	128.0	84149421	6328284206	542604498	555988086	13	-8.3	128.7	10474531739	3158342140525	49459904633	E
96	-29.8	147.2	201164702	11882850022	4501243923	4375182735	220	-30.1	149.7	13702674269	1831669964644	52016978068	E
171	-21.3	-5.3	51471447808	7549380842062	176743110693	1035198695083	140	-19.9	-2.9	3437356502	1464448780733	10626445666	A

[a] Coupled systems removed from consideration for Figures S4 and S5. See Supplementary Text S1 for more information.

Table S4. Summary of all model outputs used in this work, with a total of 16 scenarios from four climate model studies.

Study/Model	Scenario	Location in Figure 4
Wordsworth et al. (2015)	Rainfall (1 bar, solar flux=764.5 W m^{-2})	b (rain)
	Snowfall (0.4 bar, solar flux=441.1 W m^{-2})	b (snow)
Kamada et al., (2020)	0.5 bar	c (0.5 bar)
	1.0 bar	c (1.0 bar)
	1.5 bar	c (1.5 bar)
	2.0 bar	c (2.0 bar)
Guzewich et al. (2020)	10 m GEL[a], obliquity=25°	d (25°) & e (10 m GEL)
	10 m GEL, obliquity=45°	d (45°)
	10 m GEL, obliquity=0°	d (0°)
	100 m GEL, obliquity=25°	e (100 m GEL)
	100 m GEL, obliquity=0°	-
	500 m GEL, obliquity=25°	e (500 m GEL
Steakley et al., (2019)	1 bar, 50 km-impactor, RAC[b]	f (50 km)
	1 bar, 50 km-impactor, RIC[b]	-
	1 bar, 100 km-impactor, RAC	f (100 km)
	150 mbar, 100 km-impactor, RIC	-

[a]GEL = global equivalent layer; [b]RAC = radiatively active clouds; RIC = radiatively inert clouds.